

1 **Electrification Within Wintertime Stratiform Regions Sampled During the**
2 **2020/2022 NASA IMPACTS Field Campaign**
3

4 **Sebastian S. Harkema^{1†}, Lawrence D. Carey¹, Christopher J. Schultz², Edward R.**
5 **Mansell⁴, Emily B. Berndt², Alexandre O. Fierro⁵, Toshi Matsui^{6,7}**

6 ¹Department of Atmospheric and Earth Science, University of Alabama in Huntsville,
7 Huntsville, AL

8 ²Earth Science Branch, NASA Marshall Space Flight Center, Huntsville, AL

9 ⁴NOAA/National Severe Storms Laboratory, Norman, OK

10 ⁵Metocean Team, I&E Engineering, BP Exploration and Operating Company, Ltd., Sunbury,
11 United Kingdom

12 ⁶Mesoscale Atmospheric Processes Laboratory, NASA Goddard Space Flight Center, Greenbelt,
13 MD

14 ⁷Earth System Science Interdisciplinary Center, University of Maryland, College Park, MD

15
16 Corresponding author: Sebastian Harkema (sebastian.harkema@nasa.gov)

17 [†]Corresponding author address: Department of Atmospheric and Earth Science, University of
18 Alabama in Huntsville, 320 Sparkman Dr. NW, Huntsville, AL 35899

19 **Key Points:**

- 20 • Electrification within wintertime stratiform regions were associated with collisions
21 between large non-rimed ice and snow hydrometeors
- 22 • For the first time, large-scale electrification was simulated for two nor'easters to provide
23 context to aircraft in-situ observations
- 24 • Snow hydrometeors were found to carry more charge density, compared to graupel, in
25 simulated wintertime stratiform regions
- 26
27
28
29

30 **Abstract**

31 Two nor'easter events – sampled during the NASA Investigation of Microphysics and
32 Precipitation for Atlantic Coast-Threatening Snowstorms (IMPACTS) field campaign – were
33 examined to characterize the microphysics in relation to the underlying electrification processes
34 within wintertime stratiform regions. A theoretical model was developed to determine whether
35 accretion or diffusion growth regimes were preferential during periods of greatest electrification.
36 Model simulation with electrification parameterization was used to provide supplemental context
37 to the physical processes of in-cloud microphysics and electrification. The strongest electric fields
38 (i.e., $\sim 80 \text{ V m}^{-1}$ at 20 km) during the 2020 NASA IMPACTS deployment was associated with
39 large non-rimed ice crystals colliding with each other. During the 29-30 January 2022 science
40 flight, the NASA P-3 microphysical probe data demonstrated that non-inductive charging was
41 possible off the coastline of Cape Cod, Massachusetts. Later in the science flight, when the NASA
42 P-3 and ER-2 were coordinating with each other, measured electric fields consistently were less
43 than 8 V m^{-1} and electrification was subdued owing to reduced concentrations of graupel and large
44 ice hydrometeors. Altogether, the in-situ observations provide evidence for the non-riming
45 collisional charging mechanism and demonstrates that graupel and supercooled liquid water may
46 not be necessary for weak electrification within wintertime stratiform regions. Model output from
47 simulation of both events suggested that the main synoptic snowbands were associated with
48 elevated hydrometeor snow charge density and electric fields.

49 **Plain Language Summary**

50 Cloud particle probe data and numerical weather prediction output were examined to understand
51 the potential electrification processes for two winter storms that impacted the Northeast region of
52 the United States. During the 07 February 2020 event, the greatest observed electrification was

53 associated with pristine ice crystals and large snowflakes in an environment with little to no liquid
54 water and high collision rates between large ice crystals. Electrification was likely during the
55 earlier stages of the 29-30 January 2022 event – via collisions of graupel and ice hydrometeors in
56 the presence of supercooled liquid water – but became subdued later in the flight due to the reduced
57 number of graupel and ice crystals within the cloud structure. The numerical weather prediction
58 model output from the two events suggested that snow carries the most electrical charge in
59 wintertime stratiform regions.

60 **1 Introduction**

61 Cloud electrification must occur on two spatial scales: 1) small scales that electrify
62 individual hydrometeors, and 2) large scales (~5 km) that effectively separates the charges on
63 larger and smaller particles by differential sedimentation. The most widely accepted mechanism
64 for in-cloud electrification is the charge separation that occurs when ice crystals collide with
65 graupel in the presence of supercooled liquid water (SCLW). “Non-inductive” means that the
66 process is not dependent on a pre-existing electric field (Reynolds et al., 1957). Hydrometeor
67 sedimentation serves as the large-scale mechanism responsible for large scale charge separation;
68 whereby relatively fast-falling hydrometeors (i.e., graupel) transfer charge via rebounding
69 collision with ice crystals, and then fall out relative to the crystals (Williams & Lhermitte, 1983;
70 Williams, 1985). Laboratory studies have long supported the importance of charge separation from
71 collisions of graupel with ice crystals when SCLW is present in the initial build-up of electric
72 fields in thunderclouds (e.g., Takahashi, 1978; Saunders et al., 2006). At temperatures lower than
73 -10°C , hydrometeor collisions leave graupel with either positive or negative charge, depending on
74 the cloud water content (Takahashi, 1978; Saunders & Peck, 1998; Saunders et al., 2006).
75 Laboratory studies have also shown that at warm temperatures between -10°C and -2°C , graupel

76 usually gains positive charge. A so-cold “reversal temperature” may denote the switch between
77 negative and positive charging of graupel, depending on the cloud water content (Jayaratne et al.,
78 1983; Takahashi et al., 1999).

79 When comparing the riming (i.e., accretion) and completely glaciated environments,
80 Jayaratne et al., (1983) demonstrated that charge transfers on graupel particles were a magnitude
81 less in non-riming environments, non-supersaturated, compared to riming environments. Other
82 laboratory studies have examined non-riming environments and found weak charge transfer (Baker
83 et al., 1987; Caranti et al., 1991; Gaskell & Illingworth, 1980; Saunders et al., 2001). Luque et al.,
84 (2016) determined that the charge separated per collisions in non-riming conditions with ice
85 supersaturation were on the same order of magnitude for ice-ice collisions within riming
86 conditions. Using airborne observations, Dye & Bansemer, (2019) confirmed previous
87 speculations – from Dye & Willett, (2007) – that electric fields (i.e., 10-30 kV m⁻¹) were generated
88 via ice-ice collisions occurring in non-riming environments of stratiform regions of thunderstorms
89 in Florida. Charge separation within this region was inferred from increased/sustained electric
90 fields when ice crystals – growing by deposition – collide without SCLW being present and
91 charging within this region was not dependent on the electrification processes near the melting
92 layer. It should be noted that the non-inductive charging mechanism can occur within riming and
93 non-riming environments. Therefore, and hereafter, whenever riming and non-riming collision
94 mechanism is mentioned, it is with the understanding that it is technically the non-inductive
95 charging mechanism in riming and non-riming environments, respectively.

96 Studies that have examined the electrification processes in winter weather have
97 predominately focused on storms that develop near the Sea of Japan (e.g., Brook et al., 1982;
98 Kitagawa & Michimoto, 1994; Takahashi et al., 1999; Takeuti et al., 1978; Zheng et al., 2019).

99 Within the United States, most studies have examined winter weather electrification through the
100 use of lightning and radar datasets to provide insight into in-cloud processes or to provide
101 situational awareness for operational forecasters (Harkema et al., 2019, 2020; Market et al., 2002,
102 2006; Market & Becker, 2009; Rauber et al., 2014; Schultz et al., 2018). Kumjian & Deierling
103 (2015) used dual polarization radar and lightning mapper array measurements to infer
104 microphysical content in regions in which lightning was observed. In most cases, graupel was
105 detected but one case did not suggest graupel, thus suggesting that non-riming electrification might
106 have occurred. Furthermore, Harkema et al., (2022) examined geostationary satellite imagery to
107 infer microphysical changes at cloud top and determined that glaciation and ice collisions and/or
108 gravitational sedimentation occurred prior to lightning initiation when the surface experienced
109 snowfall.

110 Rust & Trapp, (2002) examined the electric field and diagnosed charge structure of six
111 winter nimbostratus clouds using in-situ balloon observations. Three of the cloud structures were
112 associated with snowfall at the surface and charging aloft. Furthermore, wintertime stratiform
113 regions generally had regions of positive charge over regions of negatively charged hydrometeors
114 (Rust & Trapp, 2002; Schultz et al., 2018). During the NASA Investigation of Microphysics and
115 Precipitation for Atlantic Coast-Threatening Snowstorms (IMPACTS; McMurdie et al., 2022)
116 field campaign, the Lightning Instrument Package (LIP; Bateman et al., 2007; Koshak et al., 2006;
117 Mach et al., 2020; Mach & Koshak, 2007) was deployed on the NASA ER-2. Schultz et al., (2021)
118 found that electric field measurements – sampled at an altitude of ~20 km – from NASA IMPACTS
119 were as high as 80 V m⁻¹ above non-lightning producing winter clouds and were horizontally co-
120 located with in-situ observations with periods of ice supersaturation and enhancements of SCLW.
121 Electrification was also observed in non-riming environments and provides support to the non-

122 riming collision mechanism (Dye & Bansemer, 2019). Furthermore, Schultz et al. (2021)
123 determined that these enhanced electric fields coincide with observed in-cloud electrification as
124 evident in differential reflectivity depolarization streaks (e.g., Kumjian, 2013). However, Schultz
125 et al., (2021) did not quantitatively examine their results with respect to ice crystal growth regimes,
126 hydrometeor collision rates, and the underlying ice crystal concentrations collected during the field
127 deployments.

128 The availability of NASA IMPACTS field campaign observations provides an unparalleled
129 opportunity to investigate the role of SCLW on the electrification processes within heavy-banded
130 snowfall structures. Understanding these electrification processes within winter storms also has
131 implications towards a larger understanding of electrification within stratiform regions associated
132 with severe convective weather. Therefore, the questions this study addressed were: 1) Is it
133 possible to determine if an environment is primarily associated with either the riming or non-
134 riming collision mechanisms from in-situ microphysical probe data? 2) How important is the
135 presence of SCLW and graupel for electrification within wintertime stratiform regions? 3) Is

136 graupel necessary to produce any electrification within wintertime stratiform regions? The
137 objectives of this manuscript are:

138 1) Develop a theoretical model that can differentiate non-riming (i.e., diffusion) and riming
139 (i.e., accretion) ice crystal growth regime environments using NASA IMPACTS microphysical
140 probe data;

141 2) Quantitatively examine the above theoretical model in relationship to observed SCLW
142 and the presence of graupel and relate them to the electric field measurements from LIP;

143 3) Simulate the two nor'easter events using a numerical weather prediction model that uses
144 an explicit electrification parameterization.

145 **2 Data and Methods**

146 2.1 Lightning Instrument Package

147 The seven rotating vane electric field mills mounted on the body of the NASA ER-2 aircraft
148 during the NASA IMPACTS field campaign were employed to determine the electric fields in the
149 x-, y-, and z-directions as well as the electric field produced by charge on the aircraft itself. These
150 electric field mills are collectively known as the LIP. Rapid changes of the electric field usually
151 indicate the presence of lightning. In controlled laboratory settings, these field mills were shown
152 to be sensitive to within a precision of $\pm 1.9 \text{ V m}^{-1}$ to 1.1 MV m^{-1} (Mach et al., 2009). Between the
153 2020 and 2022 NASA IMPACTS deployments, the LIP hardware was updated to increase electric
154 field sensitivity down to 1 V m^{-1} resolution, reduce power consumption, and minimize data storage

155 footprint on the host aircraft (Mach et al., 2022). It should be noted that all electric field
156 measurements were taken at the sampling altitude of the ER-2 (i.e., ~20 km or ~50 hPa).

157 2.2 The P-3 Orion In-Situ Probes

158 In-situ microphysical instrumentation were attached to the body of NASA's P-3 Orion for
159 the NASA IMPACTS field campaign and generally sampled cloud structure between -18°C and -
160 4°C. The Rosemount icing detector (RICE) was one of these instruments and provided
161 observations of SCLW and is associated with a noise level of about 0.002 g m^{-3} (Heymsfield &
162 Miloshevich, 1989). RICE does not directly measure the amount of SCLW but provides a signal
163 that it exists. The RICE probe oscillates ice-free at a standby frequency of 40 kHz and decreases
164 when SCLW accretes on the probe. When 0.5 mm of ice is accumulated on the probe, it is heated
165 for 5 s followed by a 5-10 s cool down period so that SCLW can again accrete on the probe
166 (Bansemer et al., 2020). The Droplet Measurement Technologies' Cloud Droplet Probe (CDP)
167 from the University of North Dakota was also mounted on the P-3 and can directly estimate LWC
168 from droplet size and concentration and has been shown to have less bias in LWC measurements
169 compared to other instrumentation in mixed phase and low liquid water environments (Cober et
170 al., 2001; Delene & Poellot, 2020; Lance et al., 2010).

171 The Stratton Park Engineering Company's two-dimensional stereo probe (2D-S) and
172 Hawkeye Cloud Particle Imager (CPI) provide direct quantitative values to the particles within the
173 cloud (Bansemer et al., 2020). The 2D-S is an imager that consists of two diode arrays with a
174 spatial resolution of $10 \text{ }\mu\text{m}$ per pixel and thus provide shadow images of particles in the vertical
175 and horizontal orientation. As a result, the 2D-S imagery can be used to estimate particle size
176 distribution (PSD) characteristics (e.g., total hydrometeor collision rate). Thus, the examination of
177 the PSD provides additional context to the microphysics-electrification processes within stratiform

178 regions/winter storms (Dye & Bansemer, 2019). The Hawkeye CPI also provides imagery of
 179 particles but with higher spatial resolution of 2.3 μm per pixel (Bansemer et al., 2020). This high-
 180 resolution imagery can capture individual hydrometeors and provide a context to hydrometeor type
 181 (e.g., column, dendrite, rimed ice crystal), and therefore does not estimate PSD characteristics. It
 182 should also be mentioned that a 10 second rolling mean was applied to all P-3 observation
 183 measurements.

184 2.3 Theoretical Accretional versus Diffusional Growth

185 The riming collision mechanism is dependent on the fact that graupel, ice crystals, and
 186 SCLW must coexist in the mixed-phase region of a cloud; however, how important is SCLW to
 187 electrification processes? Riming collision mechanism occurs – in part – because ice crystals grow
 188 via collection of SCLW droplets (Eq. 1):

$$189 \left(\frac{dm}{dt}\right)_{\text{accretion}} = \bar{E}M\pi R^2v \quad (1)$$

190 where the left-hand side of Eq. 1 represents the mass growth rate of an ice crystal via accretion
 191 (riming), \bar{E} is the collection efficiency, M is liquid water content (LWC), R is the ice particle radius,
 192 v is the ice particle fall speed (Rogers & Yau, 1989). In contrast, water vapor is used to grow ice
 193 crystals via diffusion (Eq. 2):

$$194 \left(\frac{dm}{dt}\right)_{\text{diffusion}} = \frac{4\pi C(S_i-1)}{\left[\left(\frac{L_s}{R_v T} - 1\right)\frac{L_s}{KT} + \frac{R_v T}{e_i D}\right]} \quad (2)$$

195 where the left-hand side of Eq. 2 represents the mass growth rate of an ice crystal via diffusion, C
 196 is the capacitance (shape) parameter, S_i is supersaturation with respect to ice, L_s is the latent heat
 197 of sublimation, R_v is the gas constant of water vapor, T is temperature, K is the coefficient of
 198 thermal conductivity of air, e_i is saturated vapor pressure of ice, D is the coefficient of diffusion of

199 water vapor in air. It should be noted that Eq. 2 neglects the kinematic effects on ice crystal growth
 200 via diffusion (Rogers & Yau, 1989).

201 Jensen & Harrington, (2015) developed a single-particle growth model to examine the
 202 growth characteristics caused by vapor growth and riming and builds on previous laboratory
 203 studies that examined environments with different levels of LWC (Takahashi et al., 1991;
 204 Takahashi & Fukuta, 1988). Figure 1 in Jensen & Harrington, (2015) hypothesized that a LWC
 205 threshold could separate preferred accretional and diffusional ice crystal growth regimes. This
 206 theoretical LWC threshold would provide insight into the extent that SCLW plays in the
 207 electrification process via riming collision (Reynolds et al., 1957) and the non-riming collision
 208 (Dye & Bansemer, 2019) mechanisms. Although it is assumed within this analysis, change in ice
 209 crystal growth regime does not necessarily mean that the change in charge separation is at the same
 210 limit as that differentiating particle growth. As a result, the theoretical LWC threshold can be
 211 calculated by setting Eq. 1 and 2 equal to each other and solving for M (i.e., LWC):

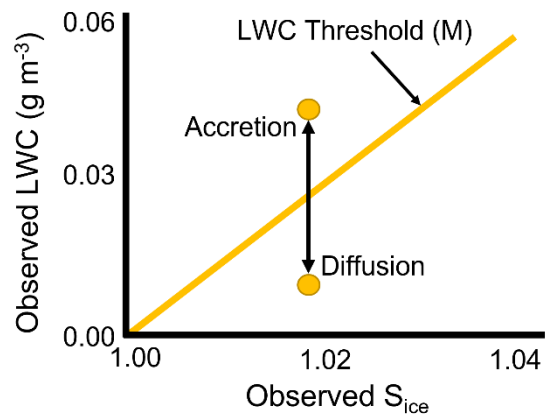
212
$$M = \frac{4C(S_i - 1)}{\bar{E}R^2v \left[\left(\frac{L_s}{R_vT} - 1 \right) \frac{L_s}{KT} + \frac{R_vT}{e_iD} \right]} \quad (3)$$

213 Note the linear relationship between the M (i.e., LWC threshold) and S_i (i.e., ice supersaturation).
 214 Collection efficiency (\bar{E}) is a function of ice particle size, the cloud droplet size, and the relative
 215 velocity between them. Furthermore, the velocity (v) is a function of the size and shape of the ice
 216 particles as well as the environment conditions, while the shape parameter (C) is related to the
 217 major and minor axes of the particle. When S_i is < 1 (i.e., environment is subsaturated with respect
 218 to ice), Eq. 3 produces a negative value for M which has no physical meaning. Therefore, negative
 219 values of M values were set to zero before any analysis. It was assumed that any ice crystal with a
 220 shape parameter could be associated with a circular cross-sectional area. For example, a regular
 221 hexagon plate ice crystal was assumed to be a circle with some depth. This is an adequate

222 assumption given that this is a simple theoretical model that ignores kinematic effects. Figure 1 is
223 a schematic that demonstrates the linearity of the derived LWC threshold when compared to ice
224 supersaturation for the accretion versus diffusion growth regimes and is based on general ice
225 crystal shape in Table 1 that were used to parameterize the theoretical LWC model. More
226 specifically, it demonstrates that for two observed LWC values (i.e., one on either side of the LWC
227 threshold) associated with the same ice supersaturation, the ice crystal growth regime will be
228 different based on the deviation from the theoretical LWC threshold value. Therefore, an observed
229 LWC greater (less) than this theoretical LWC threshold value would favor ice crystal mass growth
230 in the accretion (diffusion) regime.

231

232 **Figure 1:** Schematic that highlights the linear
233 relationship between the theoretical LWC threshold
234 and observed ice supersaturation. The mass of
235 hydrometeors with a positive or negative deviation in
236 observed LWC off the yellow line would be growing



237 faster via accretion or diffusion growth processes, respectively.

238

Ice Crystal Habit	C-axis (C)	A-axis (A)	Modeled Shape
Needle	15	1	Needle
Plate/Dendrite	1	9	Thin Plate
Column	5	2	Column
Graupel	2	3	Oblate Spheroid

239 **Table 1:** Ice crystal habits – and associated characteristics – that were used in the theoretical ice
 240 crystal growth regime model. The C- and A-axis are related to the prism and basal face of the ice
 241 crystals. For example, for a needle ice crystal, the C-axis is related to the prism length and for a
 242 plate ice crystal, the A-axis is related to the radius of the basal face.

243

244 2.4 Ice Hydrometeor Collision Rate

245 Another key component of non-inductive charging is hydrometeor collision rate, which
 246 can be used as a proxy for small-scale charge separation between hydrometeors. For a given PSD,
 247 the total collision rate can be calculated using Eq. 4 (Dye & Bansemer, 2019):

$$248 \quad C_T = \frac{1}{2} \sum_D \sum_d C_{D,d} \quad (4)$$

249 where $C_{D,d}$ is the collision rate between large (i.e., D) and small (i.e., d) particles over the entire
 250 PSD and can be calculated using Eq. 5 (Dye & Bansemer, 2019).

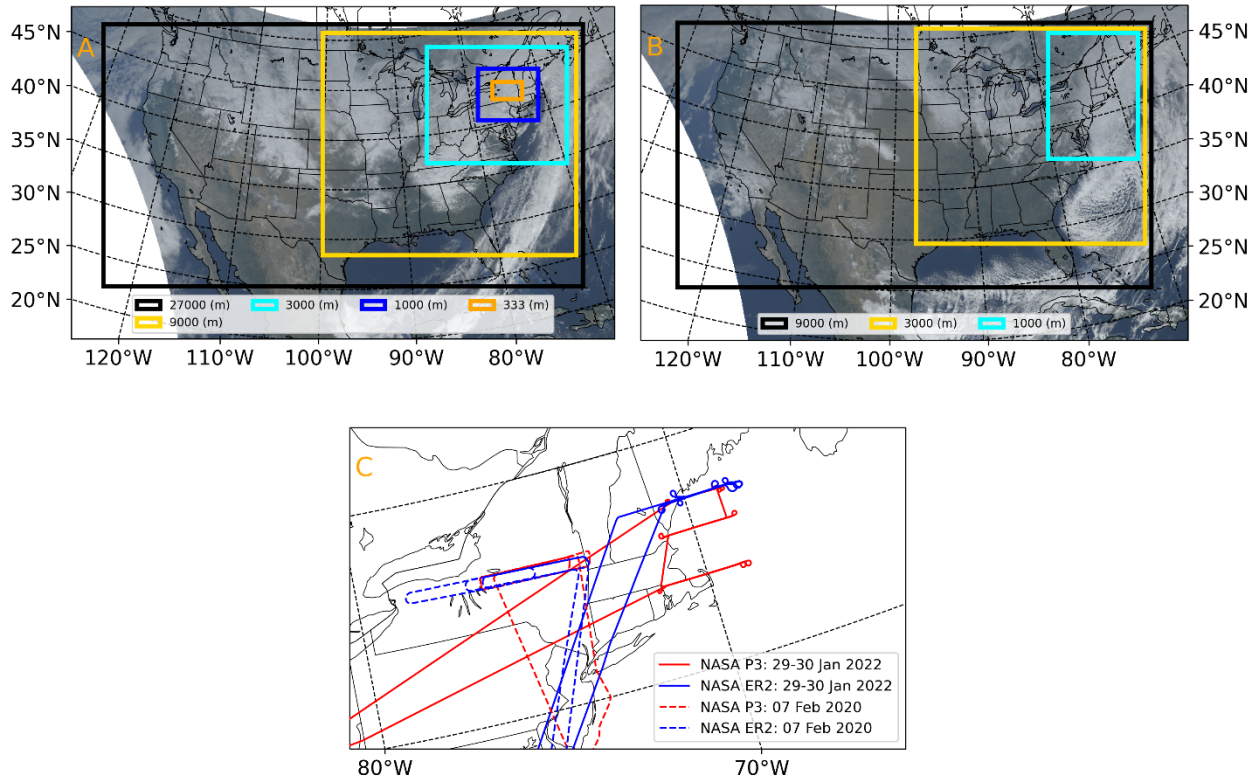
$$251 \quad C_{D,d} = \frac{\pi}{4} N_D N_d E (D + d)^2 (V_D - V_d) \quad (5)$$

252 where N_x and V_x are the concentration and terminal fall speeds of the large and small particles,
 253 respectively; E is the collision efficiency; and $(D + d)^2$ is the cross-sectional area.

254 Using the methodology from Dye & Bansemer, (2019), total collision rate was calculated
255 using Eq. 4 with an assumed perfect collision efficiency (i.e., $E=1$). An assumed perfect collision
256 efficiency represents a best-case scenario connecting the charging processes that may have
257 occurred in the environment that was being sampled by the P-3. The terminal velocity of the
258 hydrometers was estimated following the methodology described in Heymsfield & Westbrook,
259 (2010). Terminal velocities are a function of area ratio, hydrometeor diameter and mass, and
260 environmental characteristics (e.g., density of air), all of which could be derived from P-3
261 observational data. Furthermore, the crystal with sector-like branching mass-diameter relationship
262 was used to estimate ice hydrometer mass for the terminal velocity calculations (Mitchell, 1996;
263 Pruppacher & Klett, 1978). Several ice particle types from Mitchell (1996) were tested but the

264 crystal with sector-like branching produced the most realistic terminal fall speeds with respect to
 265 the NASA IMPACTS microphysical probe data.

266



267

268 **Figure 2:** Configuration of the NU-WRF-ELEC model-simulation for the a) 07 February 2020 and
 269 b) 29-30 January 2022 NASA IMPACTS science flights. The colored boxes represent the
 270 individual domains for each of the simulations. The background is Geostationary Operational
 271 Environmental Satellite – East true color imagery at 1801 UTC on 07 Feb 2020 and 29 January

272 2022, respectively. c) The flight tracks for the ER-2 (blue) and P-3 (red) for the respected science
 273 flights.

274

275 2.5 Numerical Weather Prediction Modeling

276 To provide additional context to the NASA IMPACTS observations, the NASA Unified
 277 Weather Research and Forecasting with the electrification parameterization (NU-WRF-ELEC;
 278 Skamarock & Klemp, 2008; Fierro et al., 2013; Peters-Lidard et al., 2015; Mansell et al., 2005)
 279 was used to produce simulations for the two nor'easters. Seven different model configurations for
 280 the 07 February 2020 event were quantitatively compared to observed reflectivity structures via
 281 contour frequency by altitude diagram analysis. This sensitivity testing including changing the
 282 planetary boundary layer, longwave/shortwave radiation, and convective schemes. Figure 2
 283 demonstrates the final model spatial domain configurations for the 07 February 2020 and 29-30
 284 January 2022 cases, respectively.

285

Parameters/case	07 February 2020	29-30 January 2022
ΔX (m)	~333	1000
N_z	70	70
$N_x \times N_y$	1000 x 565	1000 x 1402
dt (s)	~0.37	~1.67
Boundary Layer Scheme	YSU	YSU
Radiation Scheme	RRTMG	RRTMG
Microphysics Scheme	NSSL two-moment	NSSL two-moment
Land Surface Model	Noah	Noah
Initial-Boundary Conditions	HRRR (v3)	HRRR (v4)

286 **Table 2.** Summary of key physical and numerical parameterizations of the innermost domain for
 287 the two winter storm cases. The variables ΔX , N_z , $N_x \times N_y$, and dt are the horizontal grid spacing,

288 number of vertical layers, number of grid points in the zonal and meridional directions, and
289 computational time step, respectively.

290

291 For the 07 February 2020 simulation, the innermost domain had a grid spacing of ~333m centered
292 over New York State; in contrast; the 29-30 January 2022 simulation's innermost domain had a
293 grid spacing of 1000m centered over New England (Table 2). The latter simulation has a coarser
294 inner domain grid spacing owing to the larger area of interest demonstrated by the aircraft flight
295 lines (Fig. 2c). Table 2 also contains additional information regarding parameterizations used in
296 the model configuration.

297 The NU-WRF-ELEC simulations used the National Severe Storms Laboratory (NSSL)
298 two-moment bulk microphysics scheme (Mansell et al., 2010), which predicts the mass mixing
299 ratio and number concentration for six hydrometeor types (i.e., droplets, rain, ice crystals, snow,
300 graupel, and hail). Graupel and hail further have predicted mean particle density. All hydrometeor
301 classes have predicted charge density through various charging processes and mass transfers
302 between species (Mansell et al., 2005). Inductive charging were parameterized via Mansell et al.,
303 (2005) and non-inductive charging was parameterized using the modified Saunders & Peck, (1998)
304 scheme (Mansell et al., 2010). Furthermore, charge can be distributed and separated throughout
305 the system via the continuity equation for charge on hydrometeors (Eq. 6; Mansell et al. 2005):

306
$$\frac{\partial \rho_n}{\partial t} = -\nabla \cdot (\rho_n V) + \nabla \cdot (K_h \nabla \rho_n) + \frac{\partial (v_{t,n} \rho_n)}{\partial z} + S_n \quad (6)$$

307 where the left-hand side represents the net charge budget tendency on a given hydrometer type,
308 and the right-hand terms represent advection of charge transport (including resolved turbulent
309 eddies), subgrid turbulent mixing, hydrometeor sedimentation, and local sink and source terms.
310 These terms are not explicitly found within the WRF-ELEC model output. Brothers et al., (2018)

311 expanded Eq. (6) in their model simulations and determined that lightning deposition,
312 sedimentation, and non-inductive charging tendencies contributed most to the charge budget of
313 simulated summer convective storms. The bulk lightning discharge scheme (adapted from Ziegler
314 & MacGorman, 1994) was implemented for both simulations (Fierro et al., 2013). Essentially, this
315 lightning parameterization produces a cylindrical discharge when the electric field exceeds a
316 critical threshold (Dwyer, 2003). Following the methods of Ziegler et al., (1991), a screening layer
317 was applied to all clear air/cloud boundaries. It should be mentioned that WRF-ELEC sets charging
318 (i.e., non-inductive and inductive) to zero in environments with a rime accretion rate $< 0.1 \text{ g m}^{-2}$
319 s^{-1} (i.e., low liquid water content environments; Mansell et al., 2005, 2010; Saunders & Peck,
320 1998). As a result, WRF-ELEC cannot explicitly resolve the charging via the non-riming collision
321 mechanism.

322 **3 Analysis**

323 3.1 Riming and Non-riming Case: February 7, 2020

324 The NASA ER-2 and P-3 were sampling a rain-to-snow transition region in New York
325 State – in a coordinated race-track pattern – that was associated with a rapidly deepening cyclone
326 (Fig. 2a). Lightning flashes were observed during the 07 February 2020 snowstorm but occurred
327 outside of sampling domain for the science flights (not shown). During this science flight, LIP was
328 measuring electric fields as high as 80 V m^{-1} which were the highest recorded during the 2020
329 NASA IMPACTS field deployment (Schultz et al., 2021). Schultz et al. also determined that some
330 enhancements in electric fields were associated with non-riming environments while others
331 showed no enhanced electric fields. As a result, this case provided an ideal scenario for

332 investigating the electrification complexities associated with both riming and non-riming
333 environments.

334 Using NASA IMPACTS microphysical probe data from 1530 to 1545 UTC on 07 February
335 2020, the theoretical LWC threshold for a single column ice crystal with a radius and length of
336 0.85 mm and 2.13 mm, respectively, was calculated at four different fall speeds (Fig. 3). In an
337 environment with a LWC of $3 \times 10^{-2} \text{ g m}^{-3}$ and an ice supersaturation of 1.05 (i.e., the observation
338 within the black box), the column ice crystal could be growing in either a diffusion or accretion
339 dominant growth regime depending on the ice crystal terminal fall speed. At lower fall speeds (i.e.,
340 1 and 5 cm s^{-1}), the modeled hydrometeor would be in a diffusion dominant growth region with
341 respect to the black boxed environment in Fig. 3. In contrast, at higher fall speeds (i.e., 10 and 25
342 cm s^{-1}) the accretion growth regime would be favored for the specific modeled hydrometeor as the
343 observed LWC has a positive deviation off the theoretical LWC threshold. From an electrification
344 perspective, the faster falling column ice crystal would theoretically be charging – in that instant
345 in time – via the riming collision mechanism because the column ice crystal was collecting more
346 SCLW and colliding with smaller crystals. Whereas the non-riming collision mechanism would
347 be favored at lower fall speeds because the column ice crystal was growing faster via diffusion at

348 that instant in time. Although it is assumed in this analysis, it should be noted that any changes in
 349 ice crystal growth regime may not be at the same limit with regards to changes in charge separation.

350

351

352 **Figure 3:** Observed ice supersaturation

353 and LWC values (blue dots) between

354 1530 and 1545 UTC on 07 February

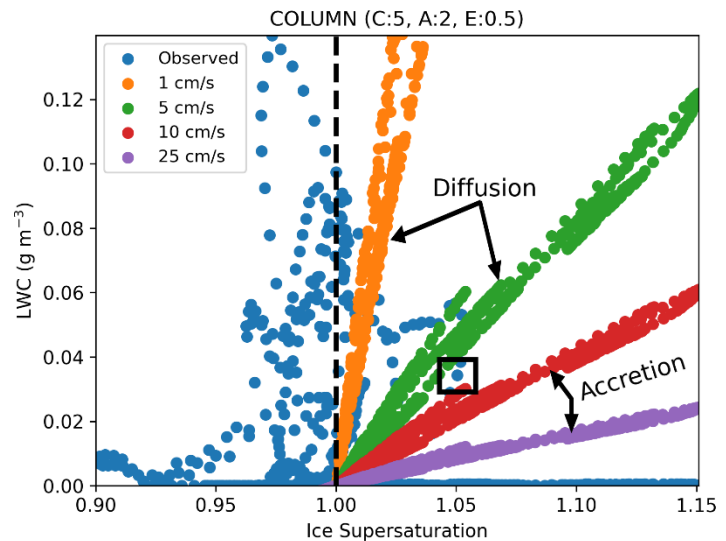
355 2020. The black box represents the

356 potential environment of interest.

357 Assuming a column ice particle with a

358 radius and length of 0.85 mm and 2.13

359 mm, respectively and a collection



360 efficiency of 0.5. The non-blue colored dots represent the theoretical LWC threshold based on

361 observed ice supersaturation at four different terminal fall speeds. Diffusional growth will be

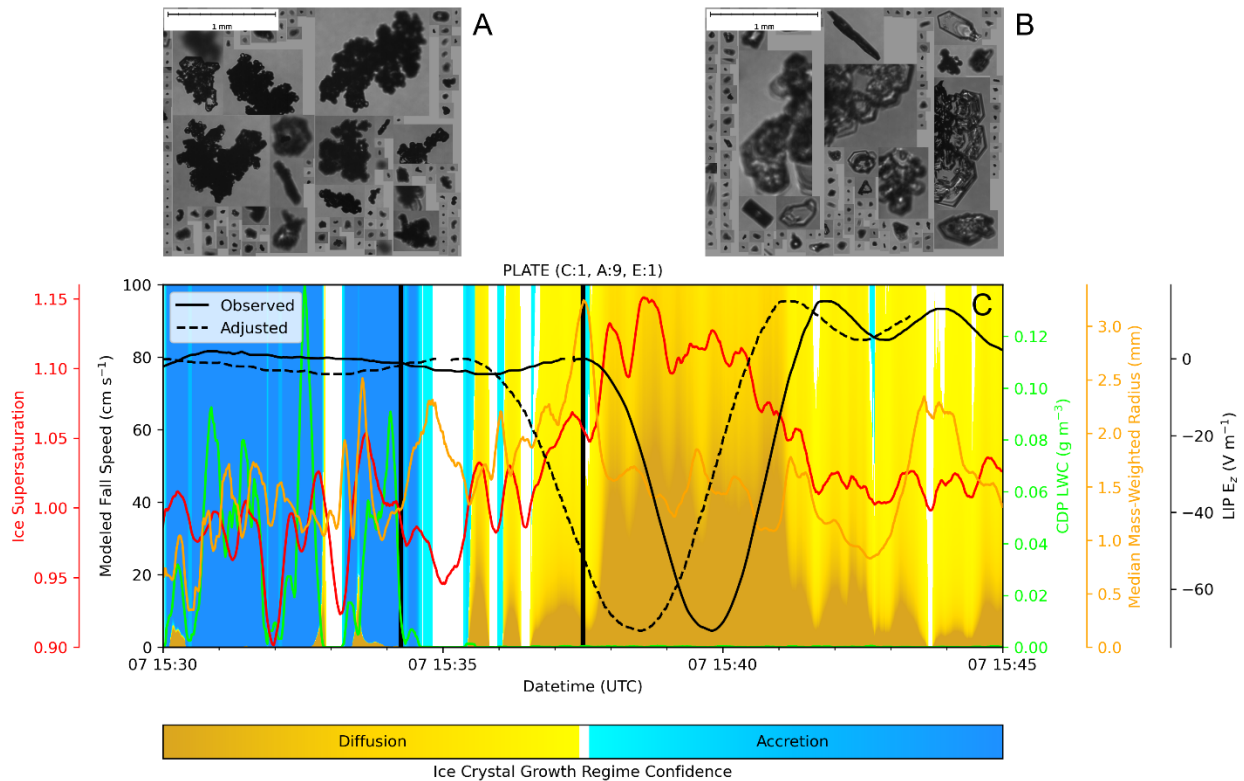
362 favored with lower fall speeds and accretional growth with higher fall speeds with respect to the

363 black boxed environment. The vertical black dashed line represents 100% ice supersaturation and

364 provides insight into sublimation (ice supersaturation < 100%) and diffusion (ice supersaturation
 365 $\geq 100\%$) environments.

366

367



368

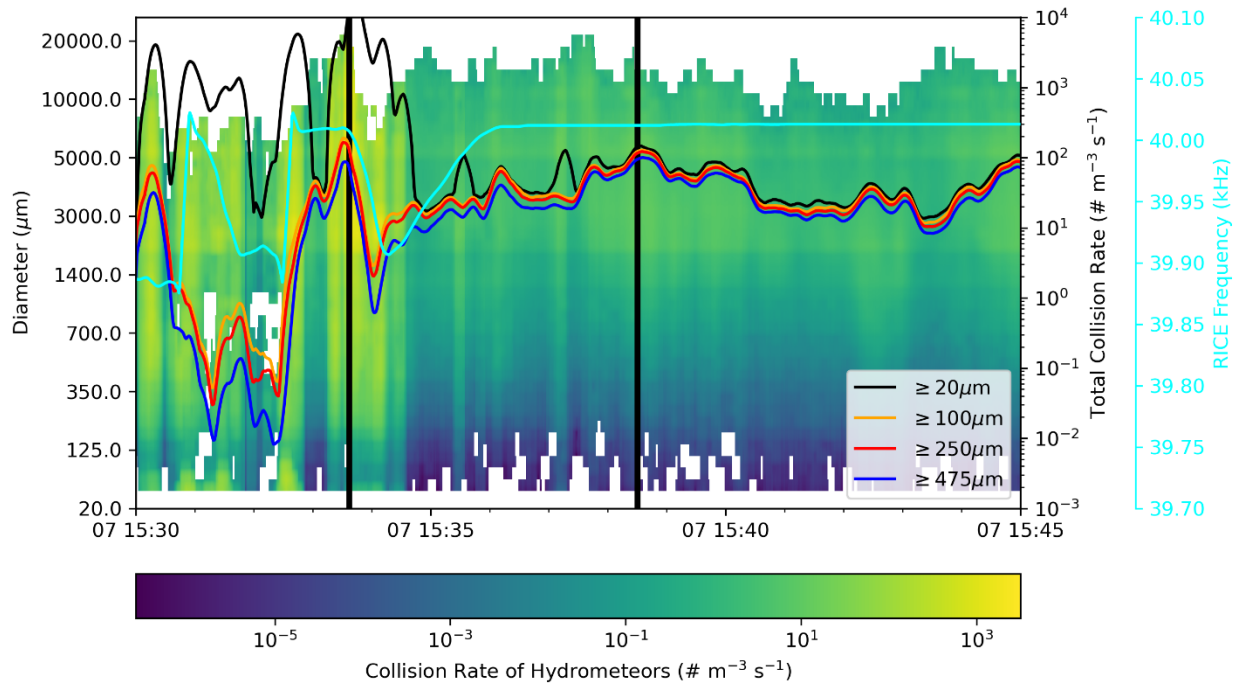
369 **Figure 4:** a) Rimed ice crystals (1534:15 UTC) and b) Pristine ice crystals (1537:30 UTC)
 370 observed by the CPI on 07 February 2020 (times denoted by thick vertical lines on panel c); c)
 371 Modeled variation of a modeled plate ice crystal with a collection efficiency of one, C-axis and A-
 372 axis of one and nine, respectively. The primary y-axis represents modeled terminal fall speeds of
 373 a modeled plate ice crystal. The ice crystal growth regime based on the theoretical LWC, observed
 374 LWC (lime green line) and ice supersaturation (red line), and median mass-weighted hydrometeor

375 radius (orange line). Black lines represent LIP observations while the dashed line represents the
376 spatiotemporally adjusted electric fields to account for offsets between the NASA ER-2 and P-3.

377
378 Between 1530 and 1545 UTC on 07 February 2020, the P-3 was flying at an altitude of
379 approximately 3.6 km while sampling a rain-to-snow transition region. The sampled
380 environmental temperature in the rain (snow) region was approximately -6°C (-10°C). During this
381 period, the CPI onboard the P-3 showed that ice hydrometeors were heavily rimed at the
382 beginning of the flight leg and became less rimed (i.e., more pristine) as the aircraft traversed west
383 across the rain-to-snow transition region (Fig. 4a,b). The theoretical ice crystal growth regime
384 model for a plate ice crystal match with the CPI observations while the P-3 transitioned between
385 riming to non-riming environments when the collection efficiency was assumed to be one (Fig.
386 4c). See the supplemental material to see how the theoretical model output changes when different
387 collection efficiencies were used. The shading in the background represents deviation (orange =
388 negative, blue = positive) from the theoretical LWC threshold (i.e., M) based on the calculated
389 LWC from CDP (lime green line), the median mass-weighted ice hydrometeor radius from 2D-S
390 (orange line), and ice supersaturation (red line) at various terminal fall speeds between 0 and 100
391 cm s^{-1} . Fig. 4c also contains z-direction electric field measurements from LIP (solid black line)
392 and an adjusted electric field to account for spatiotemporal differences between the ER-2 and P-3
393 (dashed black line). Between 1530 and 1535 UTC, the CDP LWC values were as high as 0.14 g m^{-3}
394 m^{-3} but generally hovered between 0.02 and 0.1 g m^{-3} . The decrease in CDP LWC after 1535 UTC
395 coincides with the P-3 crossing the rain region to the snowy region of the system. During this time,
396 the microphysical probe data estimated an overall increase in median mass-weighted ice
397 hydrometeor radius from 0.74 to 2.02 mm and z-direction electric fields were on the order of 10

398 V m^{-1} or less. Enhancements in ice supersaturation can occur during periods with relatively high
399 LWC. As a result, the theoretical model suggests that ice crystals will be growing faster via
400 diffusion at lower terminal fall speeds even when LWC was relatively high. The theoretical model
401 estimated with reasonable confidence that accretion was the dominant growth regime for the
402 median ice crystal because of the elevated LWC values. In contrast, the theoretical model estimated
403 that the dominant growth regime between 1535 and 1545 UTC was diffusion except at higher
404 terminal fall speeds and generally matches the CPI imagery (Fig. 4b,c). Furthermore, the
405 theoretical model indicated several periods of time where it had little-to-no confidence in either
406 accretion or diffusion being the dominant growth regime at the various modeled fall speeds (i.e.,
407 all white background throughout the y-axis model fall speeds; Fig. 4c). More specifically, there
408 were entire periods when the theoretical model was not defining a dominant growth regime for
409 any modeled fall speed (e.g., 1535 UTC). Interestingly, this time was associated with derived CDP
410 LWC values $\ll 0.01 \text{ g m}^{-3}$ and ice supersaturation as low as 0.94. As a result, the theoretical model
411 could be suggesting that this timeframe was associated with an environment that was favoring
412 sublimation compared to accretion and diffusion. This becomes more evident when the collection
413 efficiency was decreased (see the supplemental material). Z-direction electric fields were between
414 $\pm 12 \text{ V m}^{-1}$ and suggested that weak electrification could have been possible during periods of
415 sublimation (Fig. 4c). Even when accounting for the spatiotemporal offsets of the P-3 and ER-2,
416 the largest LIP z-direction electric fields magnitudes (i.e., $\sim 70 \text{ V m}^{-1}$) were associated with this

417 region of relatively low LWC and pristine ice crystals. It is important to note, however, that the P-
 418 3 pass is at one level, which may not necessarily be representative of the whole column.



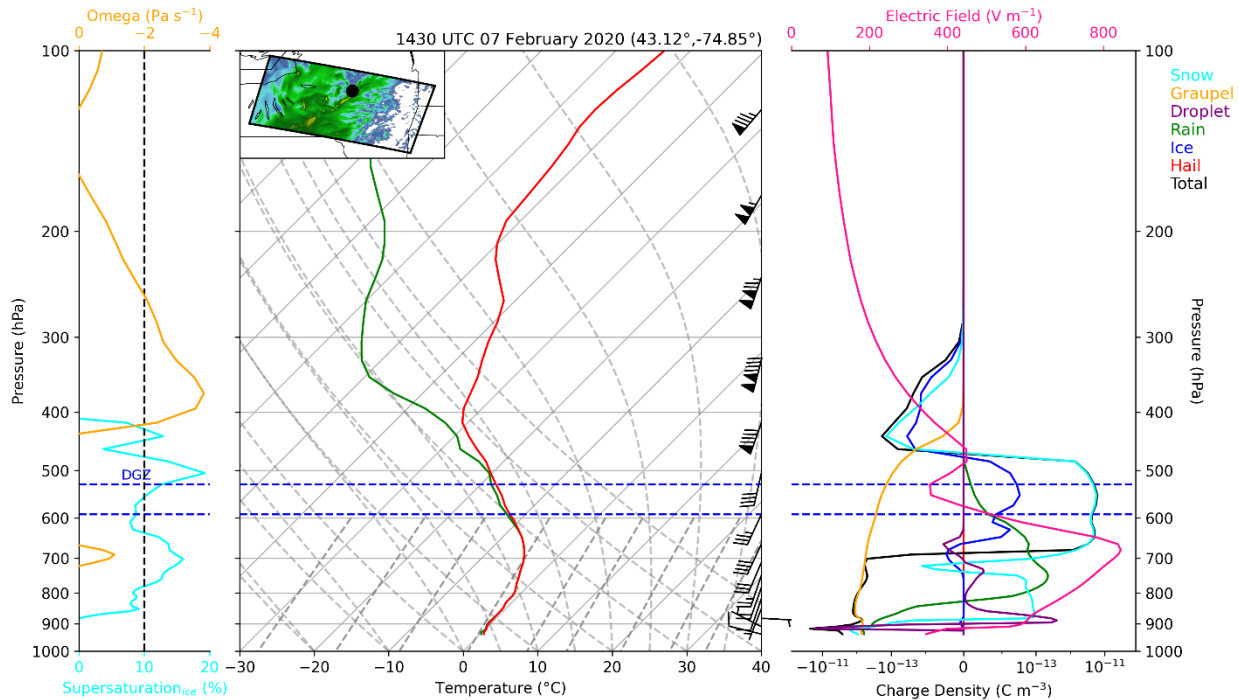
419
 420 **Figure 5:** Calculated hydrometeor collision rates (multicolored lines) and RICE frequency (cyan
 421 line) between 1530 and 1545 UTC on 07 February 2020. The ordinate (y-axis) physically
 422 represents the binned ice crystal diameters derived from the 2DS data. Background represents the
 423 calculated total collision rate associated with a particular binned ice crystal diameter. The vertical
 424 black lines represent 1533:37 and 1538:30 UTC, respectively.

425
 426 The transition from riming to non-riming environments can also be seen in the hydrometeor
 427 collision rates (Fig. 5). During periods with enhanced SCLW, the RICE frequency dropped below
 428 the 40 kHz standby frequency and was collocated with the greatest overall collision rates
 429 associated with hydrometeors with a diameter $\geq 20 \mu\text{m}$ (thin black line). At 1533:37 UTC, the
 430 collisions associated with small hydrometeors between 20 and 100 μm and all other hydrometeors

431 (i.e., $D \geq 20 \mu\text{m}$) account for 98.9% of all collisions (thick vertical black line). This is demonstrated
432 by the separation between the total collision rates when only considering certain hydrometeor
433 diameter as noted by the separation between the black and orange lines between 1530 and 1535
434 UTC (Fig. 5). Starting at 1535 UTC, the collision rates stabilized to less than $146 \text{ m}^{-3} \text{ s}^{-1}$ and was
435 associated with a RICE frequency of 40 kHz (i.e., no SCLW). Furthermore, the total collision rate
436 between all hydrometeors was dominated by larger ice hydrometeors. At 1538:30 UTC, time of
437 strongest measured adjusted electric field, the total collision rate between ice hydrometeors ≥ 250
438 μm and $\geq 475 \mu\text{m}$ accounted for 81.4% and 66.5% of the total ice hydrometeor collision rate,
439 respectively (thick vertical black line; Fig. 5). At this time, the environment was associated with a
440 total collision rate of $142 \text{ m}^{-3} \text{ s}^{-1}$ and was dominated by large ice crystals colliding with each other.
441 Therefore, the largest electric field measured during the 2020 NASA IMPACTS field campaign

442 was associated within pristine ice crystal environment without an obvious riming process. This is
 443 supported via CPI imager data and the theoretical ice crystal growth regime model (Fig. 4b,c).

444



445 **Figure 6:** NU-WRF-ELEC simulated profile at 43.12°N, -74.85°W at 1430 UTC on 07 February
 446 2020. The inset map includes simulated composite reflectivity (AGL > 2500 m) at 1430 UTC.

447

448 At 1430 UTC on 07 February 2020, the NU-WRF-ELEC simulation was associated with a
 449 pocket of elevated electric fields and hydrometeor charge densities near the rain-to-snow transition
 450 region (Fig. 6). The simulation had a deep region of ice supersaturation between 900 and 400 hPa
 451 yet this region was not coincident with stronger vertical motions. The simulation developed a
 452 saturated nearly isothermal layer between the surface and 800 hPa. Simulated electric field vertical
 453 profile peaked at 700 hPa and exceeded 800 V m⁻¹. This peak in electric field coincided with a
 454 local maximum in vertical motions. The net and individual hydrometeor charge densities were
 455 very weak, with magnitudes less than 10⁻¹¹ C m⁻³ except for a localized peak in droplet charge.

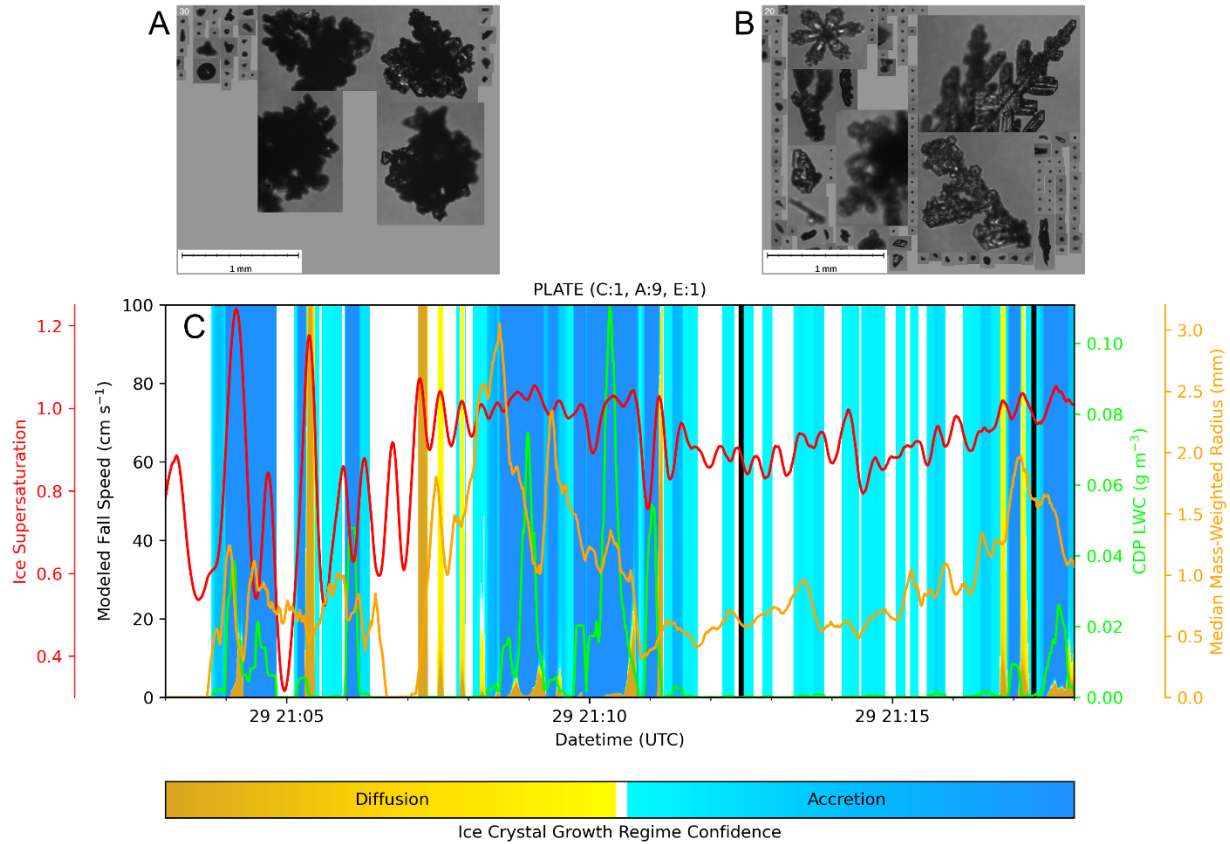
456 The droplet charge is still quite weak and likely was produced by the screening layer
457 parameterization. Even though the vertical profile was below freezing, charged rain hydrometeors
458 likely exist in the profile because they were advected from the above freezing side of the rain-to-
459 snow transition region. Furthermore, it should be mentioned that the ER-2 was not sampling this
460 location at the time; however, simulated electric field was 82 V m^{-1} at 54 hPa which was the
461 approximate pressure at which the ER-2 was sampling.

462 3.2 Large Societal Impact Case: January 29-30, 2022

463 The late January 2022 nor'easter produced copious amounts of snowfall with Plymouth,
464 Massachusetts accumulating over 61 cm of snowfall (Fig. 2b). Although thundersnow was highly
465 anticipated by forecasters and the public for this event, none was reported or observed. As a result,
466 this event served as a null case to investigate the underlying microphysics to account for the lack
467 of lightning within nor'easters that are associated with large societal impacts. From 2013 to 2354
468 UTC on 29 January 2022, the NASA P-3 was performing cross-sections sampling the snowband
469 near Cape Cod, Massachusetts and later off the coastline of Portsmouth, New Hampshire. The
470 NASA ER-2 had a delayed take-off because of airport conditions at Pope Army Airfield not
471 meeting safety guidelines, which also limited the number of coordinated P-3 and ER-2 passes.

472 From 0030 to 0147 UTC on 30 January 2022, the NASA ER-2 and P-3 flights had four coordinated
 473 legs and sampled the snowband off the Portland, Maine coastline.

474



475

476 **Figure 7:** a) Graupel (2112:30 UTC) and b) moderately rimed ice crystals (2117:20 UTC)
 477 observed by the CPI on 29 January 2022; c) Modeled variation of a modeled plate ice crystal with
 478 a collection efficiency of one, C-axis and A-axis of one and nine, respectively. The primary y-axis
 479 represents modeled terminal fall speeds of a modeled plate ice crystal. The ice crystal growth

480 regime based on the theoretical LWC, observed LWC (lime green line), ice supersaturation (red
481 line), and median mass-weighted hydrometeor radius (orange line).

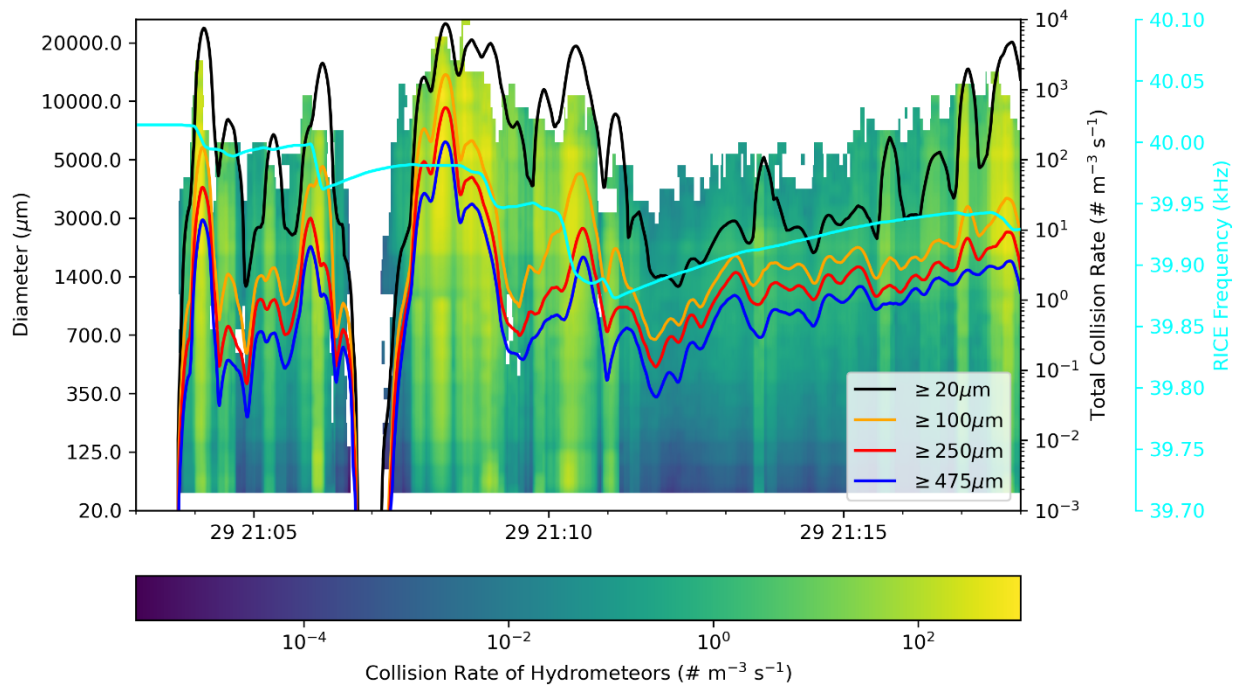
482

483 Between 2103 and 2118 UTC, the CPI indicated a rimed environment (Fig. 7a,b). Graupel
484 hydrometeors were pronounced at the beginning of this timeframe and heavily rimed sectored
485 plates became more abundant towards the end. The theoretical ice crystal growth regime suggested
486 that accretion growth would be greater than diffusional growth for much of this leg (Fig. 7c). At
487 2110:20 UTC, a peak CDP LWC of 0.11 g m^{-3} was chiefly associated with accretion (i.e., dark
488 blue background; Fig 7). In contrast, between 2111:32 and 2116:43 UTC, the CDP LWC values
489 were less than 0.01 g m^{-3} and, consequently, the theoretical model was weakly favoring an
490 accretion growth regime. This aligns with the CPI observations during this period where the
491 highest LWC values were associated with graupel hydrometeors, while the period of relatively low
492 LWC values were primarily associated with moderately rimed ice crystals. Furthermore, the
493 median mass-weighted diameter was less than 2-mm during this period of relatively low LWC.
494 Unlike the period highlighted in Fig. 4, nearly the entire time within Fig. 7 is subsaturated with
495 respect to ice (i.e., ice supersaturation < 1). As a result, the theoretical model had little-to-no
496 confidence that accretion or diffusion was the dominant growth regime (i.e., all white background
497 throughout the y-axis model fall speeds; Fig. 7) in regions that were associated with low LWCs
498 and subsaturated with respect to ice at the various modeled fall speeds. This suggests that the ice
499 crystals were sublimating faster than they were growing from accretion. Between 2104 and 2118
500 UTC (i.e., nearly the whole time of Fig. 7,8), the vibrating frequency of RICE never reached the
501 40 kHz standby vibrating frequency (Fig. 8), providing further evidence that SCLW existed during
502 this flight leg. Periods with elevated LWC values coincided with the highest total collision rates

503 (Fig. 7,8). Between 2111 and 2117 UTC, the total collision rate never exceeded $1000 \text{ m}^{-3} \text{ s}^{-1}$, which
 504 was a result of smaller hydrometeor size and lower concentrations. Although this leg had no
 505 coordination between the P-3 and ER-2 flight, the microphysical probe data supported the potential
 506 for electrification within this snowband via the riming collision mechanism (i.e., collision and
 507 presence of graupel, ice particles, and SCLW; Fig. 7,8).

508

509



510

511 **Figure 8:** Calculated hydrometeor collision rates (multicolored lines) and RICE frequency (cyan
 512 line) between 2103 and 2118 UTC on 29 January 2022. The ordinate (y-axis) physically represents

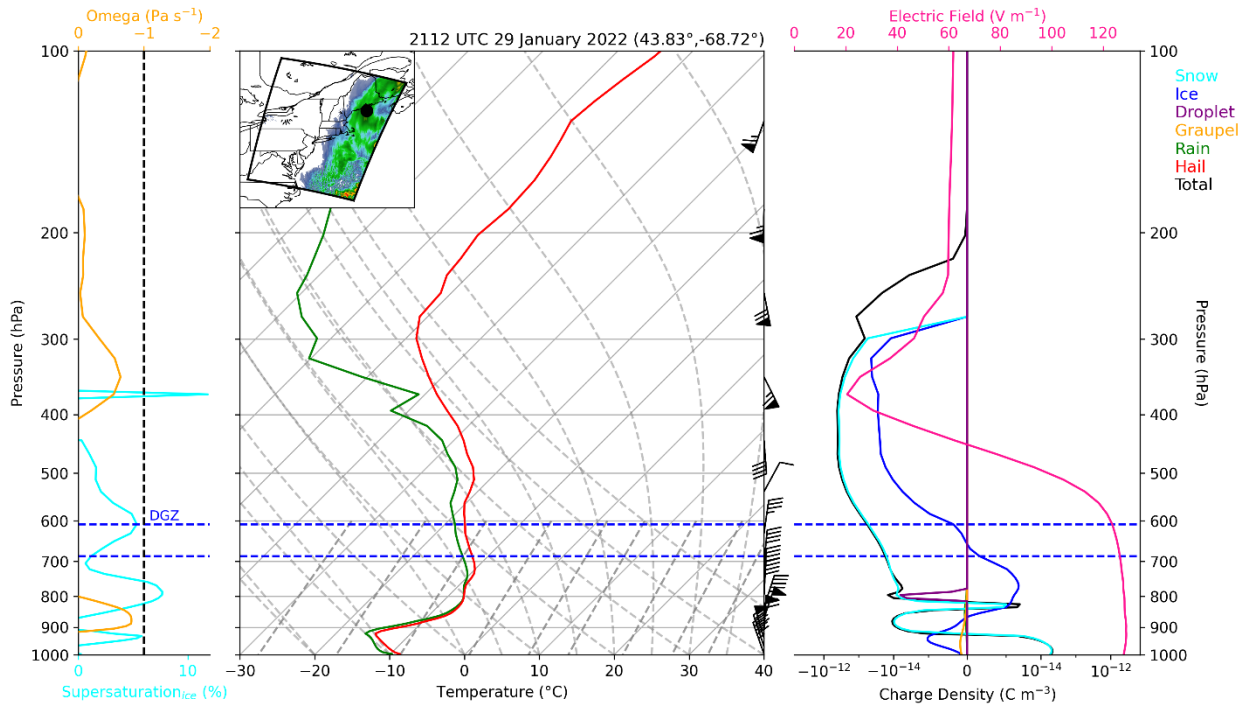
513 the binned ice crystal diameters derived from the 2D-S data. Background represents the calculated
514 total collision rate associated with a particular binned ice crystal diameter.

515

516 Even though there was no coordination between the P-3 and ER-2 between 2013 and 2354
517 UTC on 29 January 2022, the microphysical probe data do support the potential for electrification
518 via the riming collision mechanism. At 2112 UTC, the P-3 was sampling off the coast of Cape
519 Code, Massachusetts. At the same time, the NU-WRF-ELEC simulation had the main synoptic
520 snowband shifted north and offshore by approximately 100 km compared to what was observed
521 (not shown). At 2112 UTC and south of the Maine coastline, NU-WRF-ELEC simulated a layer
522 of enhanced ice supersaturation from 900 to 440 hPa (Fig. 9). The vertical profile was also
523 associated with weak vertical motions with values $> -1 \text{ pa s}^{-1}$ and no clear upward motion within
524 the dendritic growth zone. Furthermore, NU-WRF-ELEC indicated a stronger surface inversion
525 with below freezing temperatures throughout the profile. The electrification parameterization
526 produced an extremely weak charge structure with maximum charge density magnitudes less than
527 $10^{-12} \text{ C m}^{-3}$, one order of magnitude weaker compared to the 07 February 2020 simulation. The
528 electric field still appreciably exceeded typical fair-weather magnitudes and exceeded 120 V m^{-1}
529 throughout much of the lower troposphere (Fig. 9). NU-WRF-ELEC also simulated an electric
530 field of 62 V m^{-1} at $\sim 54 \text{ hPa}$ within this vertical profile. Altogether, NU-WRF-ELEC suggested

531 the potential for electrification within the main synoptic snowband prior to the sampling period of
532 the ER-2.

533



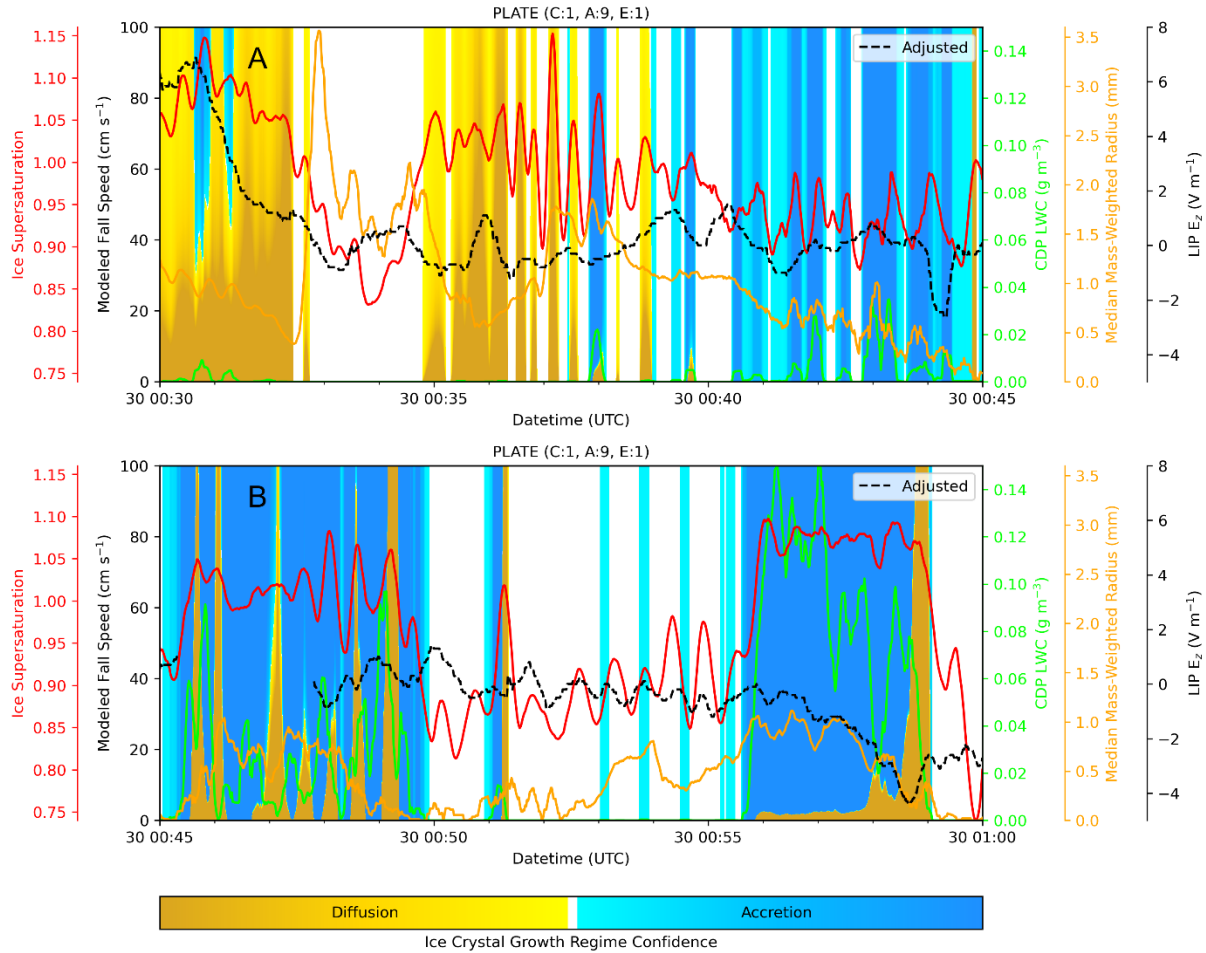
534

535 **Figure 9:** NU-WRF-ELEC simulated profile at 43.83°N, -68.72°W at 2112 UTC on 29 January
536 2022. The inset map includes simulated composite reflectivity (AGL > 500 m) at 2112 UTC.

537

538

539



540

541 **Figure 10:** Modeled variation of a modeled plate ice crystal with a collection efficiency of one,
 542 C-axis and A-axis of one and nine, respectively. The primary y-axis represents modeled terminal
 543 fall speeds of a modeled plate ice crystal. The ice crystal growth regime based on the theoretical
 544 LWC, observed LWC (lime green line), ice supersaturation (red line), and median mass-weighted
 545 hydrometeor radius (orange line) between a) 0030 and 0045 UTC and b) 0045 and 0100 UTC on
 546 30 January 2022. The black dashed line represents the spatiotemporally adjusted LIP electric fields
 547 to account for offsets between the NASA ER-2 and P-3.

548

549 The P-3 and ER-2 had two coordinated legs between 0030 and 0100 UTC on 30 January
 550 2022 off the coast of Maine. The two legs sampled the same region but sampled two different

551 microphysical environments. During the first leg (i.e., 0030-0045 UTC; Fig. 10a), CPI observed
552 both pristine and heavily rimed ice hydrometeors with the latter becoming more dominant towards
553 the second half of the flight leg (not shown). The mean median mass-weighted radius was 1.03
554 mm and was associated with a maximum CDP LWC of $3 \times 10^{-2} \text{ g m}^{-3}$ (Fig. 10a). For a modeled
555 plate ice crystal, the theoretical growth regime model suggested that sublimation was the dominate
556 regime between 0032 and 0035 UTC as the environment was subsaturated with respect to ice and
557 associated with low LWC (Fig. 10a). After 0040 UTC, the theoretical model suggested with high
558 confidence that accretion was the dominant growth regime. The second leg (i.e., 0045-0100 UTC;
559 Fig. 10b) was associated with a smaller mean median mass-weighted radius (i.e., 0.44 mm) and a
560 higher maximum LWC (i.e., 0.15 g m^{-3}). Like that in Figs. 4 and 7, little-to-no confidence of
561 accretion or diffusion growth regimes (i.e., all white background throughout the y-axis model fall
562 speeds; Fig. 10a,b) were associated with an environment with low LWC and subsaturated with
563 respect to ice. As a result, these periods of time were likely associated with ice crystals shrinking
564 via sublimation. During these periods of sublimation, z-direction electric fields varied in value
565 between -3 V m^{-1} to 1.5 V m^{-1} . The main differences between the two flight legs were caused by
566 the lower concentration of large ice particles and increased concentration of SCLW droplets.
567 Between 0045 and 0100 UTC on 30 January 2022, total collision rates associated with
568 hydrometeors $\geq 100 \mu\text{m}$ never exceeded $70 \text{ m}^{-3} \text{ s}^{-1}$. Even though SCLW was present, electrification
569 was negligible during these two flight legs because of the reduced number of ice crystals and/or

570 graupel particles. This is evident in LIP z-direction adjusted electric field as it chiefly varied
571 between -5 and 8 V m^{-1} throughout these two legs (Fig. 10a,b).

572 **4 Discussion**

573 The largest electric fields measured during the 2020 NASA IMPACTS field campaign
574 were associated with collisions between large ice particles within a non-riming environment; thus,
575 supporting the non-riming collisional mechanism for in-situ charging (Dye & Bansemer, 2019).
576 Calculated total collision rates were less than $200 \text{ m}^{-3} \text{ s}^{-1}$ at peak electrification measured by LIP
577 (i.e., 80 V m^{-1}) on 07 February 2020; in contrast, Dye & Bansemer, (2019) calculated that collision
578 rates exceeded $500 \text{ m}^{-3} \text{ s}^{-1}$ during periods of strong electrification within a Florida stratiform
579 region. The collision rates within this study, however, were predominately associated with larger
580 ice hydrometeors; whereas collisions associated with smaller hydrometeors dominated the
581 collision rate within Dye & Bansemer, (2019). Furthermore, the collision rates at peak
582 electrification were for a single flight leg and may not represent the full depth of the cloud. It
583 should also be noted the Dye and Bansemer (2019) included observations from six electric field
584 mills within the cloudy region while the LIP mills sampled the electric field above cloud top.

585 The vast majority of laboratory studies that have examined electrification mechanisms have
586 focused on collisional charging between riming graupel and ice/snow crystals (e.g., Brooks et al.,
587 1997; Jayaratne et al., 1983; Saunders et al., 2006; Saunders & Peck, 1998; Takahashi, 1978). The
588 in-situ observations of Takahashi et al., (1999) showed the electric charge carried by graupel
589 pellets and ice crystals within thunderstorm and non-thunderstorm cases for varying PSD spectra.
590 Although not explicitly discussed in their research, their Figure 16 suggests that ice crystals have
591 the potential for carrying more charge compared to graupel (of similar size) especially when the
592 diameters of the hydrometeors are smaller than 0.7 mm . This result generally matches the

593 physically-based simulation from the NU-WRF-ELEC, which highlighted that graupel may not
594 always be the dominant charge carrier with wintertime stratiform regions. Additionally, it could
595 be a result of bulk classification of graupel as generally characterized by larger, fully-rimed
596 particles, and thus a failure to produce sufficient rimed particles to drive electrification.

597 Figures 6 and 9 suggest the NU-WRF-ELEC simulations produced measurable electric
598 fields (i.e., $> 100 \text{ V m}^{-1}$) for the 07 February 2020 and 29-30 January 2022 cases. Furthermore, 54
599 hPa simulated electric fields in those vertical profiles were approximately 80 and 60 V m^{-1} ,
600 respectively. These magnitudes were comparable to observed electric fields on 07 February 2020
601 (Schultz et al. 2021). When examining the charging processes (i.e., non-inductive and inductive)
602 within the Fig 6 and 9 locations, both the non-inductive and inductive charge separation rates were
603 several magnitudes lower compared to the individual and total charge densities within the vertical
604 profiles. This suggests that the charges in the vertical profiles (Fig. 6, 9) were not locally generated.
605 Furthermore, it should be noted that the ER-2 was not sampling the locations of the vertical profiles
606 at their respected times. However, both vertical profiles do support the notion that the main
607 synoptic snowbands were electrified in both cases but far from supporting lightning initiation.

608 Fierro et al., (2013) simulated a winter storm in the Great Lakes region, which yielded
609 electric field magnitudes generally less than 50 V m^{-1} within the cloud structure and thus no
610 lightning. Similar results were produced within the NU-WRF-ELEC simulations within this study.
611 The largest simulated electric field magnitudes generated within snowfall regions in the 07
612 February 2020 and 29-30 January 2022 simulations were 11.6 and 18.3 kV m^{-1} , respectively –
613 much greater than the 0.1 to 0.8 kV m^{-1} of the selected profiles. The maximum snow electric field
614 on 07 February 2020 (i.e., 11.6 kV m^{-1}) was associated with a graupel charge density on the order
615 of $10^{-10} \text{ C m}^{-3}$ and a maximum vertical velocity of 7.2 m s^{-1} . In contrast, the graupel charge density

616 were on the order of 10^{-11} C m⁻³ and a maximum vertical velocity of 0.56 m s⁻¹ for the 29-30
617 January 2022 simulation. These suggests that enhanced electric fields may be possible in
618 convective non-convective snowfall regions. To the authors knowledge, this work is the first
619 showing that substantial electrification can be produced for snowstorms with electrification
620 parameterization but also not enough for lightning. This suggests potential of utilizing models
621 similar to NU-WRF-ELEC to augment our understanding of the electrification processes within
622 snowstorms (Harkema et al., 2019; Market et al., 2002; Schultz, 1999). It should also be mentioned
623 that the individual hydrometeor PSD within bulk microphysics scheme (e.g., NSSL) likely do not
624 match with those from observations from the NASA IMPACTS field campaign. As a result, any
625 electrification comparisons between the numerical model output and observations must be placed
626 within the context that there were likely inherent differences between the observed and simulated
627 hydrometeors. Analysis would be warranted to compare the NSSL PSD and those observed during
628 the NASA IMPACTS field campaign but is beyond the scope of this project.

629 **5 Conclusions**

630 Both laboratory studies and observations shows that charge separation can occur in
631 summertime stratiform regions via non-riming ice-ice collisions in summertime stratiform regions
632 with charge generated generally not depending on the melting zone (Dye & Bansemer, 2019).
633 Therefore, this study examined two nor'easters sampled during the NASA IMPACTS field
634 campaign using aircraft data to gain a better understanding of the electrification processes
635 occurring within wintertime stratiform regions. More specifically, this study examined data from
636 microphysical probes mounted onboard the NASA P-3 and established connections to the
637 theoretical electrification process (e.g., riming and non-riming collision mechanisms and ice
638 crystal growth regimes) and electric field measurements from LIP onboard the NASA ER-2

639 aircraft. A theoretical model was developed for this analysis that could quantify accretion (i.e.,
640 riming) and diffusion (i.e., non-riming) ice crystal growth regimes. NU-WRF-ELEC simulations
641 supplemented the aircraft observations and theoretical model to provide additional context to the
642 overall charge structure within wintertime stratiform regions sampled during the NASA IMPACTS
643 field campaign.

644 The chief goal of this study was to develop a method that can be used to quantify charge
645 separated regions associated with non-inductive charging within riming and non-riming
646 environments. This work focused on the importance of SCLW, graupel and hydrometeor collision
647 rates with respect to the underlying electrification potential within wintertime stratiform regions.
648 The main takeaways from this work are:

649 1) Accretion (riming) and diffusion (non-riming) growth regimes can be identified using
650 aircraft microphysical probe data and can be related to the non-inductive charging mechanism in
651 riming and non-riming environments.

652 2) Lightning within snowfall occurred outside the sampling range of the aircraft or did not
653 occur during the 07 February 2020 and 29-30 January 2022 cases, respectively. The strongest
654 electric fields from the 2020 NASA IMPACTS field deployment were associated with a non-
655 riming environment and the collision rates were dominated by collisions between large ice crystals.
656 As a result, we infer that electric fields at 20 km within wintertime stratiform regions can be
657 generated by the non-riming collision mechanism.

658 3) Weak electrification was simulated using NU-WRF-ELEC and vertical profiles of mean
659 hydrometeor charge density were examined. Electric fields as high as 800 V m^{-1} and 128 V m^{-1}
660 were simulated within the synoptic snowbands during the 07 February 2020 and 29-30 January
661 2022 cases, respectively. The modeled charging processes (i.e., non-inductive and inductive) were

662 only active for conditions of riming, which suggests that riming may be only a sufficient but not
663 necessary condition for appreciable charge separation.

664 Overall, understanding the microphysical processes within winter storms provides insight
665 into the electrification processes within stratiform regions. Furthermore, the NU-WRF-ELEC
666 simulations did not produce any lightning discharges within snowfall in either simulation. As a
667 result, a follow-up study will examine the potential of using NU-WRF-ELEC to simulate a mid-
668 latitude cyclone associated with lightning within snowfall. Furthermore, it would be advantageous
669 to perform Lagrangian analysis to track charged hydrometeors to fully understanding the physical
670 processes that may impact the charge structure in these wintertime stratiform regions.

671 **Acknowledgments**

672 This work is part of a larger investigation of electrified snowfall that is directly supported through
673 NASA's Future Investigators in NASA Earth and Space Science and Technology (FINESST)
674 program # 80NSSC20K1623. Additionally, this work was also supported by Dr. Tsengdar Lee of
675 NASA's Research and Analysis Program, Weather and Atmospheric Dynamics Focus Area, as
676 part of the Short-term Prediction Research and Transition (SPoRT) Center at Marshall Space Flight
677 Center and supported through the NASA-UAH Cooperative agreement # 80MSFC22M0004. The
678 authors would also like to thank the NASA Center for Climate Simulation for allotting
679 computational time on the Discover Supercomputer to run the two simulations. Lastly, the authors
680 want to thank Jim Dye and the two anonymous reviewers for providing valuable insight and
681 suggestions regarding the analysis of the theoretical microphysical model and NU-WRF-ELEC.

682

683 **Open Research**

684 NASA IMPACTS data used within this study can be freely obtained online from the NASA
685 Global Hydrology Resource Center Distributed Active Archive Center, Huntsville, Alabama,
686 USA (McMurdie et al., 2019). The HRRR data used to initialize the NU-WRF simulations can
687 be obtained via NOAA's Amazon Web Service (Benjamin et al., 2016; Blaylock et al., 2017;
688 accessed via <https://noaa-hrrr-bdp-pds.s3.amazonaws.com/index.html>). NU-WRF-ELEC
689 software are available in <https://nuwrf.gsfc.nasa.gov/software>.

690

691 **References**

- 692 Baker, B., Baker, M. B., Jayaratne, E. R., Latham, J., & Saunders, C. P. R. (1987). The Influence
693 of Diffusional Growth Rates On the Charge Transfer Accompanying Rebounding
694 Collisions Between Ice Crystals and Soft Hailstones. *Quarterly Journal of the Royal*
695 *Meteorological Society*, 113(478), 1193–1215. <https://doi.org/10.1002/qj.49711347807>
- 696 Bansemmer, A., Delene, D., Heymsfield, A. J., O'Brien, J., Poellot, M. R., Sand, K., & Sova, G.
697 (2020). NCAR Particle Probes IMPACTS. Dataset available online from the NASA
698 Global Hydrology Resource Center DAAC. Huntsville, AL, USA. Retrieved from
699 <http://dx.doi.org/10.5067/IMPACTS/PROBES/DATA101>
- 700 Bateman, M. G., Stewart, M. F., Podgorny, S. J., Christian, H. J., Mach, D. M., Blakeslee, R. J.,
701 et al. (2007). A Low-Noise, Microprocessor-Controlled, Internally Digitizing Rotating-
702 Vane Electric Field Mill for Airborne Platforms. *Journal of Atmospheric and Oceanic*
703 *Technology*, 24(7), 1245–1255. <https://doi.org/10.1175/JTECH2039.1>
- 704 Benjamin, S. G., Weygandt, S. S., Brown, J. M., Hu, M., Alexander, C. R., Smirnova, T. G., et
705 al. (2016). A North American Hourly Assimilation and Model Forecast Cycle: The Rapid

- 706 Refresh. *Monthly Weather Review*, 144(4), 1669–1694. <https://doi.org/10.1175/MWR-D->
707 15-0242.1
- 708 Blaylock, B. K., Horel, J. D., & Liston, S. T. (2017). Cloud archiving and data mining of High-
709 Resolution Rapid Refresh forecast model output. *Computers & Geosciences*, 109(C), 43–
710 50. <https://doi.org/10.1016/j.cageo.2017.08.005>
- 711 Brook, M., Nakano, M., Krehbiel, P., & Takeuti, T. (1982). The electrical structure of the
712 hokuriku winter thunderstorms. *Journal of Geophysical Research: Oceans*, 87(C2),
713 1207–1215. <https://doi.org/10.1029/JC087iC02p01207>
- 714 Brooks, I. M., Saunders, C. P. R., Mitzewa, R. P., & Peck, S. L. (1997). The effect on
715 thunderstorm charging of the rate of rime accretion by graupel. *Atmospheric Research*,
716 43(3), 277–295. [https://doi.org/10.1016/S0169-8095\(96\)00043-9](https://doi.org/10.1016/S0169-8095(96)00043-9)
- 717 Brothers, M. D., Bruning, E. C., & Mansell, E. R. (2018). Investigating the Relative
718 Contributions of Charge Deposition and Turbulence in Organizing Charge within a
719 Thunderstorm. *Journal of the Atmospheric Sciences*, 75(9), 3265–3284.
720 <https://doi.org/10.1175/JAS-D-18-0007.1>
- 721 Caranti, G. M., Avila, E. E., & Ré, M. A. (1991). Charge transfer during individual collisions in
722 ice growing from vapor deposition. *Journal of Geophysical Research: Atmospheres*,
723 96(D8), 15365–15375. <https://doi.org/10.1029/90JD02691>
- 724 Cober, S. G., Isaac, G. A., Korolev, A. V., & Strapp, J. W. (2001). Assessing Cloud-Phase
725 Conditions. *Journal of Applied Meteorology and Climatology*, 40(11), 1967–1983.
726 [https://doi.org/10.1175/1520-0450\(2001\)040<1967:ACPC>2.0.CO;2](https://doi.org/10.1175/1520-0450(2001)040<1967:ACPC>2.0.CO;2)

- 727 Delene, D., & Poellot, M. (2020). UND Cloud Microphysics IMPACTS. Dataset available online
728 from the NASA Global Hydrology Resource Center DAAC. Huntsville, AL, USA.
729 Retrieved from <https://doi.org/10.5067/IMPACTS/MULTIPLE/DATA101>
- 730 Dwyer, J. R. (2003). A fundamental limit on electric fields in air. *Geophysical Research Letters*,
731 *30*(20). <https://doi.org/10.1029/2003GL017781>
- 732 Dye, J. E., & Bansemer, A. (2019). Electrification in Mesoscale Updrafts of Deep Stratiform and
733 Anvil Clouds in Florida. *Journal of Geophysical Research: Atmospheres*, *124*(2), 1021–
734 1049. <https://doi.org/10.1029/2018JD029130>
- 735 Dye, J. E., & Willett, J. C. (2007). Observed Enhancement of Reflectivity and the Electric Field
736 in Long-Lived Florida Anvils. *Monthly Weather Review*, *135*(10), 3362–3380.
737 <https://doi.org/10.1175/MWR3484.1>
- 738 Fierro, A. O., Mansell, E. R., MacGorman, D. R., & Ziegler, C. L. (2013). The Implementation
739 of an Explicit Charging and Discharge Lightning Scheme within the WRF-ARW Model:
740 Benchmark Simulations of a Continental Squall Line, a Tropical Cyclone, and a Winter
741 Storm. *Monthly Weather Review*, *141*(7), 2390–2415. [https://doi.org/10.1175/MWR-D-](https://doi.org/10.1175/MWR-D-12-00278.1)
742 [12-00278.1](https://doi.org/10.1175/MWR-D-12-00278.1)
- 743 Gaskell, W., & Illingworth, A. J. (1980). Charge transfer accompanying individual collisions
744 between ice particles and its role in thunderstorm electrification. *Quarterly Journal of the*
745 *Royal Meteorological Society*, *106*(450), 841–854.
746 <https://doi.org/10.1002/qj.49710645013>
- 747 Harkema, S. S., Schultz, C. J., Berndt, E. B., & Bitzer, P. M. (2019). Geostationary Lightning
748 Mapper Flash Characteristics of Electrified Snowfall Events. *Weather and Forecasting*,
749 *34*(5), 1571–1585. <https://doi.org/10.1175/WAF-D-19-0082.1>

- 750 Harkema, S. S., Berndt, E. B., & Schultz, C. J. (2020). Characterization of Snowfall Rates,
751 Totals, and Snow-to-Liquid Ratios in Electrified Snowfall Events Identified by the
752 Geostationary Lightning Mapper. *Weather and Forecasting*, 35(2), 673–689.
753 <https://doi.org/10.1175/WAF-D-19-0126.1>
- 754 Harkema, S. S., Berndt, E. B., Mecikalski, J. R., & Cordak, A. (2022). Advanced Baseline
755 Imager Cloud-Top Trajectories and Properties of Electrified Snowfall Flash Initiation.
756 *Weather and Forecasting*, 36(6), 2289–2303. <https://doi.org/10.1175/WAF-D-21-0003.1>
- 757 Heymsfield, A. J., & Westbrook, C. D. (2010). Advances in the Estimation of Ice Particle Fall
758 Speeds Using Laboratory and Field Measurements. *Journal of the Atmospheric Sciences*,
759 67(8), 2469–2482. <https://doi.org/10.1175/2010JAS3379.1>
- 760 Heymsfield, Andrew J., & Miloshevich, L. M. (1989). Evaluation of Liquid Water Measuring
761 Instruments in Cold Clouds Sampled during FIRE. *Journal of Atmospheric and Oceanic*
762 *Technology*, 6(3), 378–388. [https://doi.org/10.1175/1520-
763 0426\(1989\)006<0378:EOLWMI>2.0.CO;2](https://doi.org/10.1175/1520-0426(1989)006<0378:EOLWMI>2.0.CO;2)
- 764 Jayaratne, E. R., Saunders, C. P. R., & Hallett, J. (1983). Laboratory studies of the charging of
765 soft-hail during ice crystal interactions. *Quarterly Journal of the Royal Meteorological*
766 *Society*, 109(461), 609–630. <https://doi.org/10.1002/qj.49710946111>
- 767 Jensen, A. A., & Harrington, J. Y. (2015). Modeling Ice Crystal Aspect Ratio Evolution during
768 Riming: A Single-Particle Growth Model. *Journal of the Atmospheric Sciences*, 72(7),
769 2569–2590. <https://doi.org/10.1175/JAS-D-14-0297.1>
- 770 Kitagawa, N., & Michimoto, K. (1994). Meteorological and electrical aspects of winter
771 thunderclouds. *Journal of Geophysical Research: Atmospheres*, 99(D5), 10713–10721.
772 <https://doi.org/10.1029/94JD00288>

- 773 Koshak, W. J., Mach, D. M., Christian, H. J., Stewart, M. F., & Bateman, M. G. (2006).
774 Retrieving Storm Electric Fields from Aircraft Field Mill Data. Part II: Applications.
775 *Journal of Atmospheric and Oceanic Technology*, 23(10), 1303–1322.
776 <https://doi.org/10.1175/JTECH1918.1>
- 777 Kumjian, M. (2013). Principles and applications of dual-polarization weather radar. Part III:
778 Artifacts. *Journal of Operational Meteorology*, 1(21), 265–274.
779 <https://doi.org/10.15191/nwajom.2013.0121>
- 780 Kumjian, M. R., & Deierling, W. (2015). Analysis of Thundersnow Storms over Northern
781 Colorado. *Weather and Forecasting*, 30(6), 1469–1490. [https://doi.org/10.1175/WAF-D-](https://doi.org/10.1175/WAF-D-15-0007.1)
782 [15-0007.1](https://doi.org/10.1175/WAF-D-15-0007.1)
- 783 Lance, S., Brock, C. A., Rogers, D., & Gordon, J. A. (2010). Water droplet calibration of the
784 Cloud Droplet Probe (CDP) and in-flight performance in liquid, ice and mixed-phase
785 clouds during ARCPAC. *Atmospheric Measurement Techniques*, 3(6), 1683–1706.
786 <https://doi.org/10.5194/amt-3-1683-2010>
- 787 Luque, M. Y., Bürgesser, R., & Ávila, E. (2016). Thunderstorm graupel charging in the absence
788 of supercooled water droplets. *Quarterly Journal of the Royal Meteorological Society*,
789 *142*(699), 2418–2423. <https://doi.org/10.1002/qj.2834>
- 790 Mach, D. M., & Koshak, W. J. (2007). General Matrix Inversion Technique for the Calibration
791 of Electric Field Sensor Arrays on Aircraft Platforms. *Journal of Atmospheric and*
792 *Oceanic Technology*, 24(9), 1576–1587. <https://doi.org/10.1175/JTECH2080.1>
- 793 Mach, D. M., Bateman, M. G., & Schultz, C. J. (2020). Lightning Instrument Package (LIP)
794 IMPACTS. Dataset available online from the NASA Global Hydrology Resource Center
795 DAAC. Huntsville, AL, USA. Retrieved from <https://10.5067/IMPACTS/LIP/DATA101>

- 796 Mach, D. M., Bateman, M., & Schultz, C. (2022). Lightning Instrument Package (LIP)
797 IMPACTS. Dataset available online from the NASA Global Hydrology Resource Center
798 DAAC. Huntsville, AL, USA. Retrieved from <https://10.5067/IMPACTS/LIP/DATA101>
- 799 Mach, Douglas M., Blakeslee, R. J., Bateman, M. G., & Bailey, J. C. (2009). Electric fields,
800 conductivity, and estimated currents from aircraft overflights of electrified clouds.
801 *Journal of Geophysical Research: Atmospheres*, *114*(D10).
802 <https://doi.org/10.1029/2008JD011495>
- 803 Mansell, E. R., MacGorman, D. R., Ziegler, C. L., & Straka, J. M. (2005). Charge structure and
804 lightning sensitivity in a simulated multicell thunderstorm. *Journal of Geophysical*
805 *Research: Atmospheres*, *110*(D12). <https://doi.org/10.1029/2004JD005287>
- 806 Mansell, E. R., Ziegler, C. L., & Bruning, E. C. (2010). Simulated Electrification of a Small
807 Thunderstorm with Two-Moment Bulk Microphysics. *Journal of the Atmospheric*
808 *Sciences*, *67*(1), 171–194. <https://doi.org/10.1175/2009JAS2965.1>
- 809 Market, P. S., & Becker, A. E. (2009). A study of lightning flashes attending periods of banded
810 snowfall. *Geophysical Research Letters*, *36*(1). <https://doi.org/10.1029/2008GL036317>
- 811 Market, P. S., Halcomb, C. E., & Ebert, R. L. (2002). A Climatology of Thundersnow Events
812 over the Contiguous United States. *Weather and Forecasting*, *17*(6), 1290–1295.
813 [https://doi.org/10.1175/1520-0434\(2002\)017<1290:ACOTEO>2.0.CO;2](https://doi.org/10.1175/1520-0434(2002)017<1290:ACOTEO>2.0.CO;2)
- 814 Market, P. S., Oravetz, A. M., Gaede, D., Bookbinder, E., Lupo, A. R., Melick, C. J., et al.
815 (2006). Proximity soundings of thundersnow in the central United States. *Journal of*
816 *Geophysical Research: Atmospheres*, *111*(D19). <https://doi.org/10.1029/2006JD007061>
- 817 McMurdie, L., Heymsfield, G., Yorks, J. E., & Braun, S. A. (2019). Investigation of
818 Microphysics and Precipitation for Atlantic Coast-Threatening Snowstorms (IMPACTS)

- 819 Collection [Data set]. Data available online [<http://ghrc.nsstc.nasa.gov/>] from the NASA
820 EOSDIS Global Hydrometeorology Resource Center Distribution Active Archive Center,
821 Huntsville, Alabama, U.S.A. <https://doi.org/10.5067/IMPACTS/DATA101>
- 822 McMurdie, L. A., Heymsfield, G. M., Yorks, J. E., Braun, S. A., Skofronick-Jackson, G.,
823 Rauber, R. M., et al. (2022). Chasing Snowstorms: The Investigation of Microphysics
824 and Precipitation for Atlantic Coast-Threatening Snowstorms (IMPACTS) Campaign.
825 *Bulletin of the American Meteorological Society*, *103*(5), E1243–E1269.
826 <https://doi.org/10.1175/BAMS-D-20-0246.1>
- 827 Mitchell, D. L. (1996). Use of Mass- and Area-Dimensional Power Laws for Determining
828 Precipitation Particle Terminal Velocities. *Journal of the Atmospheric Sciences*, *53*(12),
829 1710–1723. [https://doi.org/10.1175/1520-0469\(1996\)053<1710:UOMAAD>2.0.CO;2](https://doi.org/10.1175/1520-0469(1996)053<1710:UOMAAD>2.0.CO;2)
- 830 Peters-Lidard, C. D., Kemp, E. M., Matsui, T., Santanello, J. A., Kumar, S. V., Jacob, J. P., et al.
831 (2015). Integrated modeling of aerosol, cloud, precipitation and land processes at
832 satellite-resolved scales. *Environmental Modelling & Software*, *67*, 149–159.
833 <https://doi.org/10.1016/j.envsoft.2015.01.007>
- 834 Pruppacher, H. R., & Klett, J. D. (1978). *Microphysics of Clouds and Precipitation* (Vol. 18).
835 Kluwer Academic Publishers.
- 836 Rauber, R. M., Wegman, J., Plummer, D. M., Rosenow, A. A., Peterson, M., McFarquhar, G.
837 M., et al. (2014). Stability and Charging Characteristics of the Comma Head Region of
838 Continental Winter Cyclones. *Journal of the Atmospheric Sciences*, *71*(5), 1559–1582.
839 <https://doi.org/10.1175/JAS-D-13-0253.1>

- 840 Reynolds, S. E., Brook, M., & Gourley, M. F. (1957). THUNDERSTORM CHARGE
841 SEPARATION. *Journal of the Atmospheric Sciences*, *14*(5), 426–436.
842 [https://doi.org/10.1175/1520-0469\(1957\)014<0426:TCS>2.0.CO;2](https://doi.org/10.1175/1520-0469(1957)014<0426:TCS>2.0.CO;2)
- 843 Rogers, R. R., & Yau, M. K. (1989). *A Short Course in Cloud Physics*. Pergamon Press.
- 844 Rust, W. D., & Trapp, R. J. (2002). Initial balloon soundings of the electric field in winter
845 nimbostratus clouds in the USA. *Geophysical Research Letters*, *29*(20), 20-1-20–4.
846 <https://doi.org/10.1029/2002GL015278>
- 847 Saunders, C. P. R., & Peck, S. L. (1998). Laboratory studies of the influence of the rime
848 accretion rate on charge transfer during crystal/graupel collisions. *Journal of Geophysical*
849 *Research: Atmospheres*, *103*(D12), 13949–13956. <https://doi.org/10.1029/97JD02644>
- 850 Saunders, C. P. R., Peck, S. L., Aguirre Varela, G. G., Avila, E. E., & Castellano, N. E. (2001).
851 A laboratory study of the influence of water vapour and mixing on the charge transfer
852 process during collisions between ice crystals and graupel. *Atmospheric Research*, *58*(3),
853 187–203. [https://doi.org/10.1016/S0169-8095\(01\)00090-4](https://doi.org/10.1016/S0169-8095(01)00090-4)
- 854 Saunders, C. P. R., Bax-norman, H., Emersic, C., Avila, E. E., & Castellano, N. E. (2006).
855 Laboratory studies of the effect of cloud conditions on graupel/crystal charge transfer in
856 thunderstorm electrification. *Quarterly Journal of the Royal Meteorological Society*,
857 *132*(621), 2653–2673. <https://doi.org/10.1256/qj.05.218>
- 858 Schultz, C. J., Lang, T. J., Bruning, E. C., Calhoun, K. M., Harkema, S., & Curtis, N. (2018).
859 Characteristics of Lightning Within Electrified Snowfall Events Using Lightning
860 Mapping Arrays. *Journal of Geophysical Research: Atmospheres*, *123*(4), 2347–2367.
861 <https://doi.org/10.1002/2017JD027821>

- 862 Schultz, C. J., Harkema, S. S., Mach, D. M., Bateman, M., Lang, T. J., Heymsfield, G. M., et al.
863 (2021). Remote Sensing of Electric Fields Observed Within Winter Precipitation During
864 the 2020 Investigation of Microphysics and Precipitation for Atlantic Coast-Threatening
865 Snowstorms (IMPACTS) Field Campaign. *Journal of Geophysical Research:*
866 *Atmospheres*, 126(16), e2021JD034704. <https://doi.org/10.1029/2021JD034704>
- 867 Schultz, D. M. (1999). Lake-Effect Snowstorms in Northern Utah and Western New York with
868 and without Lightning. *Weather and Forecasting*, 14(6), 1023–1031.
869 [https://doi.org/10.1175/1520-0434\(1999\)014<1023:LESINU>2.0.CO;2](https://doi.org/10.1175/1520-0434(1999)014<1023:LESINU>2.0.CO;2)
- 870 Skamarock, W., & Klemp, J. (2008). A time-split nonhydrostatic atmospheric model for weather
871 research and forecasting applications. *J. Comput. Phys.*
872 <https://doi.org/10.1016/j.jcp.2007.01.037>
- 873 Takahashi, Tsuneya, & Fukuta, N. (1988). Supercooled Cloud Tunnel Studies on the Growth of
874 Snow Crystals between -4 and -20°C. *Journal of the Meteorological Society of Japan. Ser.*
875 *II*, 66(6), 841–855. https://doi.org/10.2151/jmsj1965.66.6_841
- 876 Takahashi, Tsuneya, Endoh, T., Wakahama, G., & Fukuta, N. (1991). Vapor Diffusional Growth
877 of Free-Falling Snow Crystals between -3 and -23°C. *Journal of the Meteorological*
878 *Society of Japan. Ser. II*, 69(1), 15–30. https://doi.org/10.2151/jmsj1965.69.1_15
- 879 Takahashi, Tsutomu. (1978). Riming Electrification as a Charge Generation Mechanism in
880 Thunderstorms. *Journal of the Atmospheric Sciences*, 35(8), 1536–1548.
881 [https://doi.org/10.1175/1520-0469\(1978\)035<1536:REAACG>2.0.CO;2](https://doi.org/10.1175/1520-0469(1978)035<1536:REAACG>2.0.CO;2)
- 882 Takahashi, Tsutomu, Tajiri, T., & Sonoi, Y. (1999). Charges on Graupel and Snow Crystals and
883 the Electrical Structure of Winter Thunderstorms. *Journal of the Atmospheric Sciences*,

- 884 56(11), 1561–1578. <https://doi.org/10.1175/1520->
885 0469(1999)056<1561:COGASC>2.0.CO;2
- 886 Takeuti, T., Nakano, M., Brook, M., Raymond, D. J., & Krehbiel, P. (1978). The anomalous
887 winter thunderstorms of the Hokuriku Coast. *Journal of Geophysical Research: Oceans*,
888 83(C5), 2385–2394. <https://doi.org/10.1029/JC083iC05p02385>
- 889 Williams, E. R. (1985). Large-scale charge separation in thunderclouds. *Journal of Geophysical*
890 *Research: Atmospheres*, 90(D4), 6013–6025. <https://doi.org/10.1029/JD090iD04p06013>
- 891 Williams, E. R. (1989). The tripole structure of thunderstorms. *Journal of Geophysical*
892 *Research: Atmospheres*, 94(D11), 13151–13167.
893 <https://doi.org/10.1029/JD094iD11p13151>
- 894 Williams, E. R., & Lhermitte, R. M. (1983). Radar tests of the precipitation hypothesis for
895 thunderstorm electrification. *Journal of Geophysical Research: Oceans*, 88(C15), 10984–
896 10992. <https://doi.org/10.1029/JC088iC15p10984>
- 897 Zheng, D., Wang, D., Zhang, Y., Wu, T., & Takagi, N. (2019). Charge Regions Indicated by
898 LMA Lightning Flashes in Hokuriku’s Winter Thunderstorms. *Journal of Geophysical*
899 *Research: Atmospheres*, 124(13), 7179–7206. <https://doi.org/10.1029/2018JD030060>
- 900 Ziegler, C. L., & MacGorman, D. R. (1994). Observed Lightning Morphology Relative to
901 Modeled Space Charge and Electric Field Distributions in a Tornadic Storm. *Journal of*
902 *the Atmospheric Sciences*, 51(6), 833–851. <https://doi.org/10.1175/1520->
903 0469(1994)051<0833:OLMRTM>2.0.CO;2
- 904 Ziegler, C. L., MacGorman, D. R., Dye, J. E., & Ray, P. S. (1991). A model evaluation of
905 noninductive graupel-ice charging in the early electrification of a mountain thunderstorm.

906 *Journal of Geophysical Research: Atmospheres*, 96(D7), 12833–12855.

907 <https://doi.org/10.1029/91JD01246>

908